

This is the peer reviewed version of the following article: Jian Zhang, Tao Wang, Darius Pohl, Bernd Rellinghaus, Renhao Dong, Shaohua Liu, Xiaodong Zhuang, Xinliang Feng. Interface Engineering of MoS<sub>2</sub>/Ni<sub>3</sub>S<sub>2</sub> Heterostructures for Highly Enhanced Electrochemical Overall Water Splitting Activity. *Angew.Chem.Int. Ed.* 2016, 55,6702 –6707, which has been published in final form at <https://doi.org/10.1002/anie.201602237>. This article may be used for non-commercial purposes in accordance with Wiley Terms and Conditions for Self-Archiving.

---

# Interface Engineering of MoS<sub>2</sub>/Ni<sub>3</sub>S<sub>2</sub> Heterostructures for Highly Enhanced Electrochemical Overall Water Splitting Activity

Jian Zhang<sup>[a]</sup>, Tao Wang<sup>[b]</sup>, Darius Pohl<sup>[c]</sup>, Bernd Rellinghaus<sup>[c]</sup>, Renhao Dong<sup>[a]</sup>, Shaohua Liu<sup>[a]</sup>, Xiaodong Zhuang<sup>[a]</sup>, Xinliang Feng<sup>\*[a]</sup>

Dedication

**Abstract:** To achieve sustainable production of H<sub>2</sub> fuel through water splitting, low-cost electrocatalysts for hydrogen evolution reaction (HER) and oxygen evolution reaction (OER) are required to replace Pt and IrO<sub>2</sub> catalysts. Here, for the first time, we present the interface engineering of novel MoS<sub>2</sub>/Ni<sub>3</sub>S<sub>2</sub> heterostructures, in which abundant interfaces are formed. For OER, such MoS<sub>2</sub>/Ni<sub>3</sub>S<sub>2</sub> heterostructures show an extremely low overpotential of ~218 mV at 10 mA cm<sup>-2</sup>, which is superior to that of the state-of-the-art OER electrocatalysts. Using MoS<sub>2</sub>/Ni<sub>3</sub>S<sub>2</sub> heterostructures as bifunctional electrocatalysts, an alkali electrolyser delivers a current density of 10 mA cm<sup>-2</sup> at a very low cell voltage of ~1.56 V. In combination with density function theory (DFT) calculations, this study demonstrates that the constructed interfaces synergistically favor the chemisorption of hydrogen and oxygen-containing intermediates, thus accelerating the overall electrochemical water splitting.

To achieve sustainable hydrogen production, electrochemical and photoelectrochemical water splitting are favorable strategies benefiting from abundant water resources and high-purity H<sub>2</sub> production.<sup>[1]</sup> Electrocatalysts are particularly vital to the hydrogen evolution reaction (HER) and oxygen evolution reaction (OER) by lowering the dynamic overpotentials.<sup>[2]</sup> Currently, Pt is the most efficient HER electrocatalyst with a near-zero overpotential, while IrO<sub>2</sub> and RuO<sub>2</sub> hold the benchmark for OER electrocatalysts.<sup>[3]</sup> However, the scarcity and high-cost of these noble metal-based electrocatalysts considerably impede their large-scale utilization in commercial electrolyzers.<sup>[4]</sup> For the HER in an alkaline solution, the kinetics are determined through a subtle balance between the water dissociation (Volmer step) and the subsequent chemisorption of the water splitting intermediates (OH<sup>-</sup> and H<sup>\*</sup>) on the surface of the HER electrocatalyst.<sup>[5]</sup> Thus, once an electrocatalyst facilitates the synergistic chemisorption of both H<sup>\*</sup> and OH<sup>-</sup> intermediates on the surface, the HER performance will be improved. Similarly, for the OER in an alkaline solution, the

chemisorption and dissociation of OH<sup>-</sup> and the yielded intermediates (OH<sup>\*</sup>, OOH<sup>\*</sup>, and H<sup>\*</sup>) on the surface of the electrocatalysts determine the water oxidation activity.<sup>[6]</sup> Therefore, the OER electrocatalysts capable of binding both the oxygen-containing and hydrogen intermediates are expected to favor the water oxidation reaction. Nevertheless, only the chemisorption free energy of hydrogen (or oxygen-containing) intermediates has been considered for developing HER (or OER) electrocatalysts thus far.<sup>[7]</sup>

Mo-based nanostructures, particularly MoS<sub>2</sub>, have been extensively investigated as HER electrocatalysts in the past.<sup>[8]</sup> Both DFT calculations and experimental investigations revealed that the undercoordinated Mo-S sites along the edges of MoS<sub>2</sub> possess high chemisorption capability for hydrogen, analogous to Pt.<sup>[9]</sup> On the other hand, earth-abundant transition metal (Fe, Co, and Ni, particularly Ni)-based sulphides,<sup>[10]</sup> oxides,<sup>[11]</sup> hydroxides,<sup>[12]</sup> layered double hydroxides (LDHs),<sup>[13]</sup> and phosphates<sup>[14]</sup> have been largely explored as OER electrocatalysts. The undercoordinated metal sites on the surface are pivotal in water oxidation because of their outstanding chemisorption of OH<sup>-</sup> and oxygen-containing intermediates. Therefore, integrating the advantages of the aforementioned HER and OER electrocatalysts to construct novel heterostructures, which possess binding affinities to both hydrogen and oxygen-containing intermediates, is extremely beneficial for enhancing the overall electrochemical water splitting activity.

In this study, for the first time, we present the interface engineering of novel MoS<sub>2</sub>/Ni<sub>3</sub>S<sub>2</sub> heterostructures on nickel foam. In the resultant MoS<sub>2</sub>/Ni<sub>3</sub>S<sub>2</sub> heterostructures, the outer MoS<sub>2</sub> nanosheets are decorated on the surface of the inner Ni<sub>3</sub>S<sub>2</sub> nanoparticles, which generates abundant interfaces. Such MoS<sub>2</sub>/Ni<sub>3</sub>S<sub>2</sub> heterostructures exhibit both highly efficient OER and HER activities in 1 M KOH solution. In particular, the OER onset potential of MoS<sub>2</sub>/Ni<sub>3</sub>S<sub>2</sub> heterostructures is as low as ~175 mV, and the OER current density reaches 10 mA cm<sup>-2</sup> at an overpotential of ~218 mV, which is superior to the previously reported OER electrocatalysts. Furthermore, utilizing the MoS<sub>2</sub>/Ni<sub>3</sub>S<sub>2</sub> heterostructure as a bifunctional electrocatalyst, an alkaline electrolyzer with a current density of 10 mA cm<sup>-2</sup> is operated at a low cell voltage of 1.56 V, which is considerably lower than that of the state-of-the-art overall water splitting electrocatalysts such as NiFe-LDH,<sup>[15]</sup> NiSe nanowires,<sup>[16]</sup> Ni<sub>2</sub>P nanoparticles,<sup>[17]</sup> and electrodeposited cobalt-phosphorous-derived films<sup>[18]</sup> (cell voltages > 1.6 V). Combined with DFT calculations, our results suggest that the established interfaces between Ni<sub>3</sub>S<sub>2</sub> and MoS<sub>2</sub> as well as the in-situ generated interfaces between NiO (surface electrochemical oxidation of Ni<sub>3</sub>S<sub>2</sub> under OER condition) and MoS<sub>2</sub> facilitate the synchronous

- [a] Dr. J. Zhang, Dr. R. Dong, Dr. S. Liu, Dr. X. Zhuang, Prof. X. Feng  
Center for Advancing Electronics Dresden (cfaed) & Department of  
Chemistry and Food Chemistry  
Technische Universität Dresden  
01062 Dresden, Germany  
E-mail: xinliang.feng@tu-dresden.de
- [b] Dr. T. Wang  
Leibniz-Institut für Katalyse, e.V.  
Universität Rostock  
18059 Rostock, Germany
- [c] Dr. D. Pohl, Dr. B. Rellinghaus  
Institute for Metallic Materials  
IFW Dresden  
01171 Dresden, Germany

Supporting information for this article is given via a link at the end of the document.

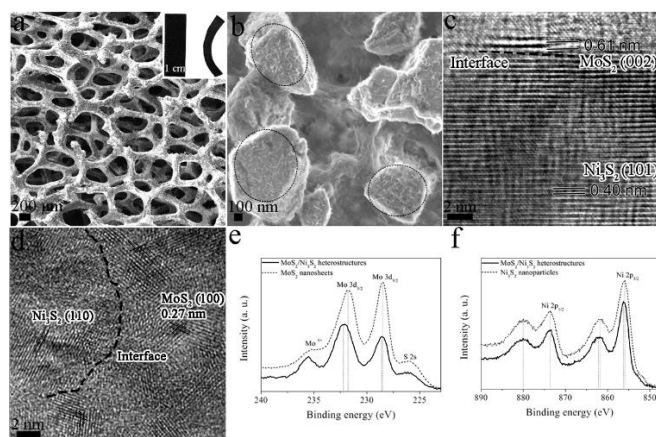


**Figure 1.** (a) and (b) scanning electron microscopy and (c) and (d) high-resolution transmission electron microscopy images of MoS<sub>2</sub>/Ni<sub>3</sub>S<sub>2</sub> heterostructures and high-resolution X-ray photoelectron spectroscopy spectrum of (e) Mo 3d and (f) Ni 2p. Inset: digital image of nickel foam coated with MoS<sub>2</sub>/Ni<sub>3</sub>S<sub>2</sub> heterostructures.

chemisorption of hydrogen and oxygen-containing intermediates, consequently improving the overall electrochemical water splitting activity.

MoS<sub>2</sub>/Ni<sub>3</sub>S<sub>2</sub> heterostructures were prepared using a commercial nickel foam (1 × 3 cm<sup>2</sup>) and (NH<sub>4</sub>)<sub>2</sub>MoS<sub>4</sub> (40 mg) through a one-pot solvothermal reaction at 200 °C for 12 h in 15 mL N, N-Dimethylformamide (DMF) (Supporting Information). During the solvothermal reaction, (NH<sub>4</sub>)<sub>2</sub>MoS<sub>4</sub> not only served as the precursor of MoS<sub>2</sub> nanosheets but also provided the sulphur source for the in-situ growth of Ni<sub>3</sub>S<sub>2</sub> nanoparticles on the nickel foam. The loading amount of MoS<sub>2</sub>/Ni<sub>3</sub>S<sub>2</sub> heterostructures on the nickel foam is approximately 9.7 mg cm<sup>-2</sup>; this value could be controlled by adjusting the amount of (NH<sub>4</sub>)<sub>2</sub>MoS<sub>4</sub> in the solution. For instance, the loading weights of MoS<sub>2</sub>/Ni<sub>3</sub>S<sub>2</sub> heterostructures were ~5.7 and ~13.1 mg cm<sup>-2</sup> when the amounts of (NH<sub>4</sub>)<sub>2</sub>MoS<sub>4</sub> were 20 and 80 mg, respectively (Figure S1–S3).

As shown in Figure 1a and the inset, the obtained nickel foam coated with MoS<sub>2</sub>/Ni<sub>3</sub>S<sub>2</sub> heterostructures has macroporous and free-standing features. The crystalline structure and surface composition of the MoS<sub>2</sub>/Ni<sub>3</sub>S<sub>2</sub> heterostructures were first confirmed through X-ray diffraction (Figure S4) and Raman spectroscopy (Figure S5) studies. To analyze the as-obtained MoS<sub>2</sub>/Ni<sub>3</sub>S<sub>2</sub> heterostructures, scanning electron microscopy (SEM) and high-resolution transmission electron microscopy (HRTEM) were used. Figure 1b reveals numerous heterostructures, which consist of inner Ni<sub>3</sub>S<sub>2</sub> nanoparticles and decorated MoS<sub>2</sub> nanosheets. The size of the Ni<sub>3</sub>S<sub>2</sub> nanoparticles was about several hundred nanometers. The size and thickness of the MoS<sub>2</sub> nanosheets were 30–130 and 5–15 nm, respectively. The element distributions of the MoS<sub>2</sub>/Ni<sub>3</sub>S<sub>2</sub> heterostructures were further analyzed through the elemental mapping of field-emission SEM (FE-SEM) (Figure S6a–d). Notably, the nickel element was mainly distributed over the nanoparticles, whereas molybdenum and sulfur were spread on and around the nanoparticles. The molar content of MoS<sub>2</sub> in MoS<sub>2</sub>/Ni<sub>3</sub>S<sub>2</sub> heterostructures was determined to be ~7.8% through energy-dispersive X-ray spectroscopy (EDX) (Figure S6e), which is

consistent with the inductively coupled plasma mass spectrometer (ICP-MS) analysis (~8.0%). We further peeled off MoS<sub>2</sub>/Ni<sub>3</sub>S<sub>2</sub> heterostructures from the nickel foam by sonication and investigated the samples by HRTEM (Figure 1c, 1d, S7 and S8). Lattice fringes with lattice distances of 0.27 and 0.61 nm corresponded to the (100) and (002) facets of MoS<sub>2</sub>, respectively, while the lattice distances of 0.40 and 0.28 nm were ascribed to the (101) and (110) facets of Ni<sub>3</sub>S<sub>2</sub>, respectively. The (002) and (100) facets of MoS<sub>2</sub> and the neighboring (101) and (110) surfaces of Ni<sub>3</sub>S<sub>2</sub> constitute the interfaces in MoS<sub>2</sub>/Ni<sub>3</sub>S<sub>2</sub> heterostructures. Next, the X-ray photoelectron spectroscopy (XPS) survey spectrum of MoS<sub>2</sub>/Ni<sub>3</sub>S<sub>2</sub> demonstrates that the chemical composition of Ni, Mo, and S is consistent with the EDX results (Figure S9). For bare MoS<sub>2</sub> nanosheets, the peaks of Mo 3d<sub>5/2</sub> and Mo 3d<sub>3/2</sub> appear at 228.5 and 231.8 eV, respectively. However, the binding energies of Mo 3d<sub>5/2</sub> and Mo 3d<sub>3/2</sub> in MoS<sub>2</sub>/Ni<sub>3</sub>S<sub>2</sub> heterostructures shift to 228.6 and 232.2 eV, respectively (Figure 1e). Similarly, the Ni 2p<sub>3/2</sub> signal in the MoS<sub>2</sub>/Ni<sub>3</sub>S<sub>2</sub> heterostructures exhibits a positive shift of ~0.3 eV relative to that in the bare Ni<sub>3</sub>S<sub>2</sub> nanoparticles (Figure 1f). These results strongly suggest the existence of strong electronic interactions between Ni<sub>3</sub>S<sub>2</sub> and MoS<sub>2</sub>, which implies the establishment of coupling interfaces.

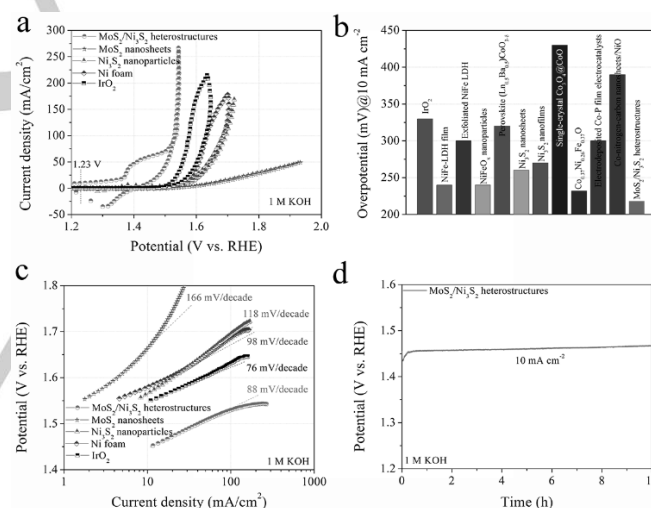


**Figure 2.** (a) CV curves and (c) related Tafel slopes of the nickel foam, MoS<sub>2</sub> nanosheets, Ni<sub>3</sub>S<sub>2</sub> nanoparticles, MoS<sub>2</sub>/Ni<sub>3</sub>S<sub>2</sub> heterostructures, and IrO<sub>2</sub>; b) OER overpotentials of the MoS<sub>2</sub>/Ni<sub>3</sub>S<sub>2</sub> heterostructures and the reported electrocatalysts for comparison at 10 mA cm<sup>-2</sup>; and d) the long-term electrochemical OER test of the MoS<sub>2</sub>/Ni<sub>3</sub>S<sub>2</sub> heterostructures at 10 mA cm<sup>-2</sup>. Electrolyte: 1 M KOH solution; CV scan rate: 1 mV s<sup>-1</sup>.

To evaluate the OER performance of the as-prepared MoS<sub>2</sub>/Ni<sub>3</sub>S<sub>2</sub> heterostructures, a three-electrode configuration was applied using an Hg/HgO electrode and a Pt rod as the reference and counter electrodes, respectively (Figure S10). The OER activities of the nickel foam, Ni<sub>3</sub>S<sub>2</sub> nanoparticles, MoS<sub>2</sub> nanosheets, MoS<sub>2</sub>/Ni<sub>3</sub>S<sub>2</sub> heterostructures, and IrO<sub>2</sub> were examined through cyclic voltammetry (CV) at a scan rate of 1 mV s<sup>-1</sup> in a 1 M KOH aqueous solution purged with O<sub>2</sub> (Figure 2a). Bare Ni<sub>3</sub>S<sub>2</sub> nanoparticles and MoS<sub>2</sub> nanosheets exhibited OER onset overpotentials of ~230 and 280 mV, respectively. By



contrast, for MoS<sub>2</sub>/Ni<sub>3</sub>S<sub>2</sub> heterostructures, oxygen generation occurred at an extremely low overpotential (~175 mV), which is considerably lower than that of commercial IrO<sub>2</sub> (~250 mV) (Figure S11 and S12). Significantly, the current density of MoS<sub>2</sub>/Ni<sub>3</sub>S<sub>2</sub> heterostructures reached 10 mA cm<sup>-2</sup> at an extremely low overpotential of ~218 mV, which outperformed IrO<sub>2</sub> (~330 mV) and the previously reported NiFe-LDH film (~240 mV),<sup>[15]</sup> (Ln<sub>0.5</sub>Ba<sub>0.5</sub>)CoO<sub>3-δ</sub> perovskite (~320 mV),<sup>[19]</sup> single-crystal Co<sub>3</sub>O<sub>4</sub>@CoO (~430 mV),<sup>[20]</sup> and electrodeposited Co-P film (~300 mV)<sup>[19]</sup> (Figure 2b).<sup>[10, 21]</sup>

Figure 2c illustrates that the Tafel slope of the MoS<sub>2</sub>/Ni<sub>3</sub>S<sub>2</sub> heterostructures is ~88 mV decade<sup>-1</sup>, which is considerably lower than that of the Ni<sub>3</sub>S<sub>2</sub> nanoparticles (~118 mV decade<sup>-1</sup>), the MoS<sub>2</sub> nanosheets (~166 mV decade<sup>-1</sup>), and the nickel foam (~98 mV decade<sup>-1</sup>). This result strongly suggests that the constructed MoS<sub>2</sub>/Ni<sub>3</sub>S<sub>2</sub> heterostructures activate water oxidation reaction kinetics. To assess the electrochemical OER stability of MoS<sub>2</sub>/Ni<sub>3</sub>S<sub>2</sub> heterostructures, a long-term water oxidation was conducted at 10 mA cm<sup>-2</sup> in 1 M KOH media. Figure 2d illustrates that the MoS<sub>2</sub>/Ni<sub>3</sub>S<sub>2</sub> heterostructures retained steady OER activity and no noticeable potential augment was observed for more than 10 h of oxygen release.

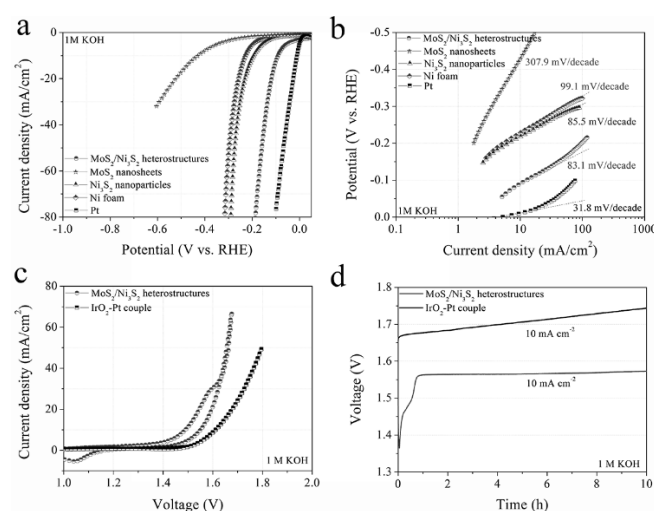


**Figure 3.** (a) Polarization curves and (b) corresponding Tafel slopes of the nickel foam, MoS<sub>2</sub> nanosheets, Ni<sub>3</sub>S<sub>2</sub> nanoparticles, MoS<sub>2</sub>/Ni<sub>3</sub>S<sub>2</sub> heterostructures, and Pt; (c) polarization curves of MoS<sub>2</sub>/Ni<sub>3</sub>S<sub>2</sub> heterostructures and IrO<sub>2</sub>-Pt couple in a two-electrode system; and (d) durable operation of the MoS<sub>2</sub>/Ni<sub>3</sub>S<sub>2</sub> heterostructures and IrO<sub>2</sub>-Pt couple at 10 mA cm<sup>-2</sup> in an alkaline electrolyzer. Electrolyte: 1 M KOH solution; CV scan rate: 1 mV s<sup>-1</sup>.

The HER activities of the as-prepared samples were evaluated in 1 M KOH electrolyte purged with N<sub>2</sub>. The polarization curves in Figure 3a show that the onset overpotentials of Ni<sub>3</sub>S<sub>2</sub> nanoparticles and MoS<sub>2</sub> nanosheets are ~120 and 236 mV, respectively. However, the onset overpotential of the MoS<sub>2</sub>/Ni<sub>3</sub>S<sub>2</sub> heterostructures substantially decreases to ~50 mV, approaching that of the Pt catalyst. At 10 mA cm<sup>-2</sup>, the applied overpotential is ~110 mV, substantially lower than that of the Ni<sub>3</sub>S<sub>2</sub> nanoparticles (~193 mV), the MoS<sub>2</sub> nanosheets (~431 mV), and the recently reported WC nanocrystals on carbon nanotubes (~150 mV),<sup>[22]</sup> CoP on carbon cloth (~209 mV),<sup>[23]</sup> MoC<sub>x</sub> nano-octahedrons

(~150 mV),<sup>[24]</sup> and cobalt-nitrogen-rich carbon nanotubes (~360 mV)<sup>[25]</sup> (Figure S13 and S14). The Tafel slopes of the MoS<sub>2</sub>/Ni<sub>3</sub>S<sub>2</sub> heterostructures, Ni<sub>3</sub>S<sub>2</sub> nanoparticles, and MoS<sub>2</sub> nanosheets are ~83, 85 and 308 mV per decade, respectively (Figure 3b). Such a Tafel slope of the MoS<sub>2</sub>/Ni<sub>3</sub>S<sub>2</sub> heterostructures suggests a combined Volmer–Heyrovsky mechanism for hydrogen production.<sup>[26]</sup> Under a cathodic current of 10 mA cm<sup>-2</sup>, there is no noticeable degradation over a 10 h galvanostatic test, which indicates an excellent electrochemical HER stability (Figure S15).

The MoS<sub>2</sub>/Ni<sub>3</sub>S<sub>2</sub> heterostructures were utilized as a bifunctional electrocatalyst for overall water splitting in a two-electrode setup in 1 M KOH solution (Figure S16). A current density of 10 mA cm<sup>-2</sup> was delivered at ~1.56 V, that is, a combined overpotential of ~330 mV for electrochemical overall water splitting (Figure 3c). Figure S17 reveals that the overall water splitting activity of the MoS<sub>2</sub>/Ni<sub>3</sub>S<sub>2</sub> heterostructures is much higher than that of the IrO<sub>2</sub>-Pt couple (~1.7 V) and other recently reported overall water splitting electrocatalysts such as NiFe-LDH (~1.7 V),<sup>[16]</sup> NiSe nanowires (~1.63 V)<sup>[17]</sup> and Ni<sub>2</sub>P nanoparticles (~1.63 V).<sup>[18]</sup> Over a 10-h galvanostatic electrolysis at 10 mA cm<sup>-2</sup>, the MoS<sub>2</sub>/Ni<sub>3</sub>S<sub>2</sub> heterostructures presented an excellent durability with negligible degradation, which is superior to that of the noble metal IrO<sub>2</sub>-Pt couple (Figure 3d). We further tested the overall electrocatalytic water splitting performance under an extremely high current density of 500 mA cm<sup>-2</sup>. Figure S18 and Movie 1 show that massive bubbles were rapidly generated on both electrodes at an applied voltage of ~1.6 V. Such a prominent performance of the constructed electrolyzer utilizing the MoS<sub>2</sub>/Ni<sub>3</sub>S<sub>2</sub> heterostructures is close to the commercial requirement of a water splitting electrolyzer (voltage ≤1.55 V at 500 mA cm<sup>-2</sup>).<sup>[27]</sup>

The nature and amount of undercoordinated metal sites are crucial for the electrochemical water splitting. The effects of the surface area on OER and HER activities of the obtained electrocatalysts were firstly studied through electrochemical double-layer capacitances (*C*<sub>dl</sub>) (Figure S19). As shown in Table S1, MoS<sub>2</sub>/Ni<sub>3</sub>S<sub>2</sub> heterostructures show a larger *C*<sub>dl</sub> (15.6 mF) than Ni<sub>3</sub>S<sub>2</sub> nanoparticles (2.1 mF) and MoS<sub>2</sub> nanosheets (8.2 mF). In sharp contrast, for OER (or HER), the current density of MoS<sub>2</sub>/Ni<sub>3</sub>S<sub>2</sub> heterostructures at 1.53 V (or -0.15 V) reached 94.8 (or 45) mA/cm<sup>2</sup>, which is substantially higher than those of Ni<sub>3</sub>S<sub>2</sub> nanoparticles (5.0 mA/cm<sup>2</sup> for OER; 4.7 mA/cm<sup>2</sup> for HER) and MoS<sub>2</sub> nanosheets (1.6 mA/cm<sup>2</sup> for OER; 2.5 mA/cm<sup>2</sup> for HER). Thereby, the greatly enhanced water splitting activities of MoS<sub>2</sub>/Ni<sub>3</sub>S<sub>2</sub> heterostructures are mainly attributed to the constructed interfaces, rather than the active surface areas.

As shown in Figure S20, the reduction and oxidation peaks of Mo<sup>5+</sup>/Mo<sup>6+</sup> ( $\epsilon > \delta \geq 4$ ) in MoS<sub>2</sub> nanosheets are located at ~0.333 and 0.449 V, while the redox reactions of Ni<sup>2+</sup>/Ni<sup>3+</sup> in Ni<sub>3</sub>S<sub>2</sub> nanoparticles occur at ~0.254 and 0.369 V. In contrast, the redox peaks in the MoS<sub>2</sub>/Ni<sub>3</sub>S<sub>2</sub> heterostructures are centered at ~0.216 and 0.489 V. These results suggest that the fabricated MoS<sub>2</sub>/Ni<sub>3</sub>S<sub>2</sub> heterostructures offer new water splitting active sites, which are endowed with the electrocatalytic properties of both Ni<sub>3</sub>S<sub>2</sub> and MoS<sub>2</sub>. The reduction peak area of MoS<sub>2</sub>/Ni<sub>3</sub>S<sub>2</sub> heterostructures is ~9.3 and 17.7 times larger than those of the Ni<sub>3</sub>S<sub>2</sub> nanoparticles and MoS<sub>2</sub> nanosheets, respectively. After the electrochemical OER process at 10 mA cm<sup>-2</sup> for 10 h in 1 M KOH solution, the structure of the MoS<sub>2</sub>/Ni<sub>3</sub>S<sub>2</sub> heterostructures was analyzed by SEM, HRTEM, XPS, element mapping and EDX, and

XPS analyses (Figure S21-S24). Notably, a thin layer of NiO with thickness of  $\sim 12.6$  nm was identified on  $\text{Ni}_3\text{S}_2$  surface, for which the lattice fringe with a lattice distance of 0.21 nm was indexed to be the (010) facet of NiO (Figure S20c). XPS result in Figure S24 further revealed the existence of NiO. The formation of NiO is due to the in-situ surface electrochemical oxidation of  $\text{Ni}_3\text{S}_2$  during the OER process which is in agreement with literature reports; and the NiO sites are electrochemically active for the OER process.<sup>10, 16</sup> Therefore, we consider that the constructed interfaces between the  $\text{Ni}_3\text{S}_2$  and  $\text{MoS}_2$  stably facilitate HER process and the interfaces between the in-situ formed NiO and  $\text{MoS}_2$  are favorable for the OER process.

To further investigate the role of the constructed interfaces in electrochemical OER and HER, the  $\text{MoS}_2/\text{Ni}_3\text{S}_2$  heterostructures with different molar contents of  $\text{MoS}_2$  have been synthesized on carbon cloth (see Experimental Section). Figure S25 shows that the OER and HER overpotentials of the bare  $\text{Ni}_3\text{S}_2$  nanoparticles and  $\text{MoS}_2$  nanosheets at  $10 \text{ mA cm}^{-2}$  are approximately 379 and 421 and 341 and 429 mV, respectively. However, the electrochemical OER and HER performances of the  $\text{MoS}_2/\text{Ni}_3\text{S}_2$  heterostructures are noticeably enhanced. When the molar content of  $\text{MoS}_2$  is  $\sim 8.3\%$ , the OER and HER overpotentials of the  $\text{MoS}_2/\text{Ni}_3\text{S}_2$  heterostructures at  $10 \text{ mA cm}^{-2}$  are as low as  $\sim 330$  and  $150$  mV, respectively. For comparison, the physically mixed  $\text{MoS}_2/\text{Ni}_3\text{S}_2$  composite (having the same chemical composition as the  $\text{MoS}_2/\text{Ni}_3\text{S}_2$  heterostructures) deliver OER and HER current densities of  $10 \text{ mA cm}^{-2}$  at overpotentials of  $\sim 356$  and  $199$  mV, respectively, which are considerably higher than those of the  $\text{MoS}_2/\text{Ni}_3\text{S}_2$  heterostructures. These results clearly manifest the crucial role of the constructed interfaces between  $\text{Ni}_3\text{S}_2$  and  $\text{MoS}_2$  as well as the interfaces between NiO and  $\text{MoS}_2$ , which are responsible for the enhanced electrochemical hydrogen and oxygen evolutions, respectively.

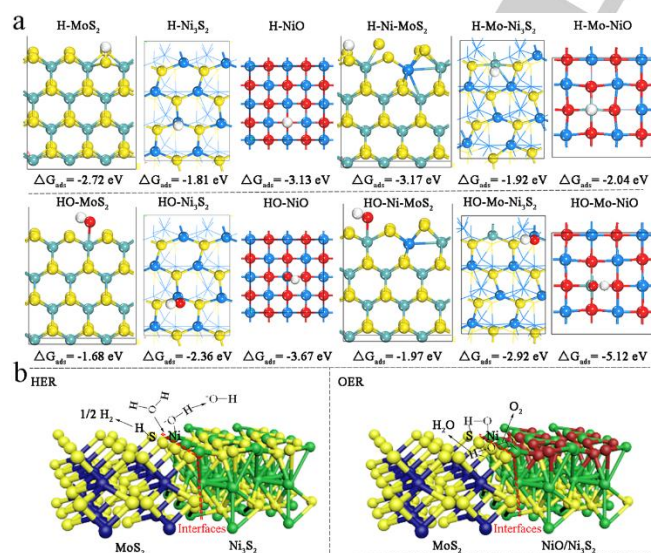


**Figure 4.** a) Chemisorption models of H and OH intermediates on the surfaces of  $\text{MoS}_2$ ,  $\text{Ni}_3\text{S}_2$ ,  $\text{MoS}_2/\text{Ni}_3\text{S}_2$  heterostructures ( $\text{Ni-MoS}_2$  and  $\text{Mo-Ni}_3\text{S}_2$  models), and  $\text{MoS}_2/\text{NiO}$  heterostructures ( $\text{Ni-MoS}_2$  and  $\text{Mo-NiO}$  models) respectively; b) the proposed mechanisms of the dissociation of  $\text{H}_2\text{O}$ , OH, and OOH intermediates on the  $\text{MoS}_2/\text{Ni}_3\text{S}_2$  heterostructures.

In order to clarify the effect of the constructed interfaces on the chemisorption of hydrogen and oxygen-containing intermediates, we utilized DFT to calculate the chemisorption free energies of hydrogen ( $\Delta G_{\text{H}}$ ) and hydroxide ( $\Delta G_{\text{OH}}$ ) on the (101) surface of  $\text{Ni}_3\text{S}_2$ , the (010) surface of NiO, and the (002) surface of  $\text{MoS}_2$ . The obtained results are described in Figure 4a. Contrary to the chemisorption on the (101) surface of  $\text{Ni}_3\text{S}_2$  ( $\Delta G_{\text{H}} = -1.81$  eV) and (002) surface of  $\text{MoS}_2$  ( $\Delta G_{\text{H}} = -2.71$  eV), H is apt to adsorb on the Mo-S edge sites of Ni-doped  $\text{MoS}_2$  model (denoted as  $\text{Ni-MoS}_2$ ) because of a lower chemisorption free energy of  $-3.17$  eV. As expected, the surface undercoordinated Ni sites of Mo-doped  $\text{Ni}_3\text{S}_2$  model (denoted as  $\text{Mo-Ni}_3\text{S}_2$ ) have a HO-chemisorption energy of  $-2.92$  eV, which is lower than the  $-1.68$  eV energy of  $\text{MoS}_2$  and  $-2.36$  eV energy of  $\text{Ni}_3\text{S}_2$ . The (101) surface of  $\text{Mo-Ni}_3\text{S}_2$  thus exhibits superior binding activity toward oxygen-containing groups. Moreover, considering the formed interfaces between  $\text{MoS}_2$  and NiO for OER, the Mo sites of the Mo-doped NiO model ( $\text{Mo-NiO}$ ) show a largely-increased HO-chemisorption energy up to  $-5.12$  eV. Accordingly, a HER mechanism on  $\text{MoS}_2/\text{Ni}_3\text{S}_2$  heterostructures and an OER mechanism on  $\text{MoS}_2/\text{NiO}$  heterostructures are proposed in Figure 4b. The constructed interfaces between  $\text{Ni}_3\text{S}_2$  and  $\text{MoS}_2$  as well as the interfaces between NiO and  $\text{MoS}_2$  have the advantages of the H-chemisorption of  $\text{MoS}_2$  and the HO-chemisorption of  $\text{Ni}_3\text{S}_2$  and NiO. As a result, the Gibbs free energies of the corresponding intermediates are efficiently decreased, facilitating the dissociation of the O-H bonds of the  $\text{H}_2\text{O}$  molecule and the OH and OOH intermediates. Eventually, the OER and HER processes are highly accelerated.

In summary, we have presented a novel approach for developing earth-abundant and high-activity overall water splitting electrocatalysts through interface engineering. The as-prepared  $\text{MoS}_2/\text{Ni}_3\text{S}_2$  heterostructures with abundant interfaces manifest excellent chemisorption abilities for both hydrogen and oxygen-containing intermediates, leading to outstanding OER and HER electrocatalytic activities in alkaline media. Therefore, the engineering and understanding of the constructed interfaces provide a favorable direction for developing low-cost and high-activity water splitting electrocatalysts, which have potential applications in photochemical, photoelectrochemical, and electrochemical  $\text{H}_2$  production and  $\text{CO}_2$  reduction.

## Acknowledgements

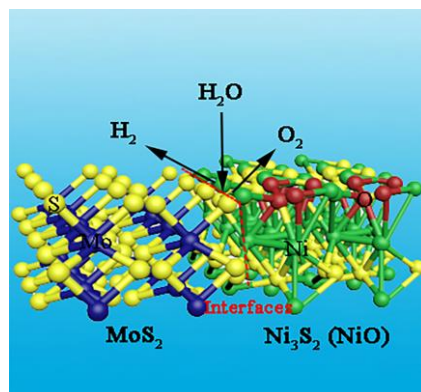
This work was financially supported by the ERC Grant on 2DMATER and EC under Graphene Flagship (No. CNECT-ICT-604391). We also acknowledge the Cfaed (Center for Advancing Electronics Dresden) and the Dresden Center for Nanoanalysis (DCN) at TU Dresden.

**Keywords:** Interface engineering • Water splitting • Electrocatalysts • Nickel sulfide • Molybdenum disulfide

- [1] J. Greeley, T. F. Jaramillo, J. Bonde, I. Chorkendorff, J. K. Nørskov, *Nat. Mater.* **2006**, 5, 909-913.
- [2] C. C. L. McCrory, S. Jung, I. M. Ferrer, S. M. Chatman, J. C. Peters, T. F. Jaramillo, *J. Am. Chem. Soc.* **2015**, 137, 4347-4357.

- [3] D. V. Esposito, S. T. Hunt, A. L. Stottlmyer, K. D. Dobson, B. E. McCandless, R. W. Birkmire, J. G. Chen, *Angew. Chem. Int. Ed.* **2010**, *49*, 9859-9862.
- [4] K. Zeng, D. Zhang, *Prog. Energy Combust. Sci.* **2010**, *36*, 307-326.
- [5] R. Subbaraman, D. Tripkovic, D. Strmcnik, K.-C. Chang, M. Uchimura, A. P. Paulikas, V. Stamenkovic, N. M. Markovic, *Science* **2011**, *334*, 1256-1260.
- [6] I. C. Man, H. Y. Su, F. Calle - Vallejo, H. A. Hansen, J. I. Martínez, N. G. Inoglu, J. Kitchin, T. F. Jaramillo, J. K. Nørskov, J. Rossmeisl, *ChemCatChem* **2011**, *3*, 1159-1165.
- [7] a) Y. Jiao, Y. Zheng, M. Jaroniec, S. Z. Qiao, *Chem. Soc. Rev.* **2015**, *44*, 2060-2086; b) ; a) J. Zhang, S. Liu, H. Liang, R. Dong, X. Feng, *Adv. Mater.* **2015**, *27*, 7426-7431; c) H.-W. Liang, S. Bruller, R. Dong, J. Zhang, X. Feng, K. Müllen, *Nat. Commun.* **2015**, *6*, 7992-7999; d) J. Wang, W. Cui, Q. Liu, Z. Xing, A. M. Asiri, X. Sun, *Adv. Mater.* **2016**, *28*, 215-230.
- [8] Y. Yan, B. Xia, Z. Xu, X. Wang, *ACS Catal.* **2014**, *4*, 1693-1705.
- [9] T. F. Jaramillo, K. P. Jørgensen, J. Bonde, J. H. Nielsen, S. Hørch, I. Chorkendorff, *Science* **2007**, *317*, 100-102.
- [10] W. Zhou, X.-J. Wu, X. Cao, X. Huang, C. Tan, J. Tian, H. Liu, J. Wang, H. Zhang, *Energy Environ. Sci.* **2013**, *6*, 2921-2924.
- [11] R. D. L. Smith, M. S. Prévot, R. D. Fagan, Z. Zhang, P. A. Sedach, M. K. J. Siu, S. Trudel, C. P. Berlinguette, *Science* **2013**, *340*, 60-63.
- [12] M. Gao, W. Sheng, Z. Zhuang, Q. Fang, S. Gu, J. Jiang, Y. Yan, *J. Am. Chem. Soc.* **2014**, *136*, 7077-7084.
- [13] C. Tang, H.-S. Wang, H.-F. Wang, Q. Zhang, G.-L. Tian, J.-Q. Nie, F. Wei, *Adv. Mater.* **2015**, *27*, 4516-4522.
- [14] M. W. Kanan, Y. Surendranath, D. G. Nocera, *Chem. Soc. Rev.* **2009**, *38*, 109-114.
- [15] J. Luo, J.-H. Im, M. T. Mayer, M. Schreier, M. K. Nazeeruddin, N.-G. Park, S. D. Tilley, H. J. Fan, M. Grätzel, *Science* **2014**, *345*, 1593-1596.
- [16] C. Tang, N. Cheng, Z. Pu, W. Xing, X. Sun, *Angew. Chem. Int. Ed.* **2015**, *127*, 9483-9487.
- [17] L.-A. Stern, L. Feng, F. Song, X. Hu, *Energy Environ. Sci.* **2015**, *8*, 2347-2351.
- [18] N. Jiang, B. You, M. Sheng, Y. Sun, *Angew. Chem. Int. Ed.* **2015**, *54*, 6251-6254.
- [19] A. Grimaud, K. J. May, C. E. Carlton, Y.-L. Lee, M. Risch, W. T. Hong, J. Zhou, Y. Shao-Horn, *Nat. Commun.* **2013**, *4*, 2439-2445.
- [20] C.-W. Tung, Y.-Y. Hsu, Y.-P. Shen, Y. Zheng, T.-S. Chan, H.-S. Sheu, Y.-C. Cheng, H. M. Chen, *Nat. Commun.* **2015**, *6*, 8106-8114.
- [21] a) F. Song, X. Hu, *Nat. Commun.* **2014**, *5*, 4477-4485; b) H. Wang, H.-W. Lee, Y. Deng, Z. Lu, P.-C. Hsu, Y. Liu, D. Lin, Y. Cui, *Nat. Commun.* **2015**, *6*, 7261-7268; c) L.-L. Feng, G. Yu, Y. Wu, G.-D. Li, H. Li, Y. Sun, T. Asefa, W. Chen, X. Zou, *J. Am. Chem. Soc.* **2015**, *137*, 14023-14026; d) W. Chen, H. Wang, Y. Li, Y. Liu, J. Sun, S. Lee, J.-S. Lee, Y. Cui, *ACS Cent. Sci.* **2015**, *1*, 244-251; e) J. Wang, K. Li, H.-x. Zhong, D. Xu, Z.-l. Wang, Z. Jiang, Z.-j. Wu, X.-b. Zhang, *Angew. Chem. Int. Ed.* **2015**, *54*, 10530-10534.
- [22] X. Fan, H. Zhou, X. Guo, *ACS Nano* **2015**, *9*, 5125-5134.
- [23] J. Tian, Q. Liu, A. M. Asiri, X. Sun, *J. Am. Chem. Soc.* **2014**, *136*, 7587-7590.
- [24] H. B. Wu, B. Y. Xia, L. Yu, X.-Y. Yu, X. W. Lou, *Nat. Commun.* **2015**, *6*, 6512-6519.
- [25] X. Zou, X. Huang, A. Goswami, R. Silva, B. R. Sathe, E. Mikmeková, T. Asefa, *Angew. Chem. Int. Ed.* **2014**, *126*, 4461-4465.
- [26] M. Gong, W. Zhou, M.-C. Tsai, J. Zhou, M. Guan, M.-C. Lin, B. Zhang, Y. Hu, D.-Y. Wang, J. Yang, S. J. Pennycook, B.-J. Hwang, H. Dai, *Nat. Commun.* **2014**, *5*, 4695-4700.
- [27] X. Lu, C. Zhao, *Nat. Commun.* **2015**, *6*, 6616-6622.

The interface engineering of novel  $\text{MoS}_2/\text{Ni}_3\text{S}_2$  heterostructures with abundant interfaces has been presented. Experimental results and DFT calculations demonstrate that the constructed interfaces synergistically favor the chemisorption of hydrogen and oxygen-containing intermediates, thus leading to highly enhanced water splitting activity.



Jian Zhang, Tao Wang, Darius Pohl, Bernd Rellinghaus, Renhao Dong, Shaohua Liu, Xiaodong Zhuang, Xinliang Feng\*

Page No. – Page No.

**Interface Engineering of  $\text{MoS}_2/\text{Ni}_3\text{S}_2$  Heterostructures for Highly Enhanced Electrochemical Overall Water Splitting Activity**